RSC Advances

PAPER

View Article Online
View Journal | View Issue

Open Access Article. Published on 28 July 2025. Downloaded on 10/26/2025 10:23:19 AM.
This article is licensed under a Creative Commons Attribution-NonCommercial 3.0 Unported Licence.

Check for updates

Cite this: *RSC Adv.*, 2025, **15**, 26660

Designing parylene coating for implantable brain–machine interfaces†

Saman Ebrahimibasabi,[a] Maryam Golshahi,[b] Naghmeh Shahraki,[b] Delaram Tamjid Shabestari,[b] Mostafa Sajjadi,[b] Seyedamin Hashemi,[c] Austin Borchert,[a] Ian Baker,[a] Layla Khalifehzadeh*[d] and Hamed Arami *[a]

Parylene is widely recognized as an effective candidate for encapsulating implantable bioelectronics due to its outstanding chemical stability, conformity and biocompatibility. However, its weak adhesion to inorganic substrates remains a significant challenge. Here, we explored various pre- and post-deposition treatments to enhance adhesion and stability of parylene coating for implantable brain–machine interfaces (BMIs). We utilized 0%, 0.5%, 1%, and 1.5% (v/v) 3-(trimethoxysilyl)propyl-methacrylate as an adhesion promoter for substrate treatment prior to deposition. Deposited samples were subsequently subjected to post-heat treatments at various temperatures. Samples were exposed to an *in vitro* accelerated aging bath at 87 °C for 7 days to assess their post-implantation durability. Cytotoxicity and *in vivo* biocompatibility were also investigated to further evaluate biocompatibility and encapsulation efficiency of parylene coatings on commonly used rigid and flexible bioelectronic substrates. The emergence of carboxyl groups in FTIR and chlorine abstraction in EDS analyses, indicated that the as-deposited samples were degraded during aging. The chemical stability of these coatings was improved in heat-treated samples due to their higher crystallinity. Additionally, delamination and microcrack initiation/growth reduced due to post-heat treatments. We found the optimal heat treatment temperature to be 150 °C; any increase beyond this compromised coating quality by increasing delamination and defect formation. Increasing the concentration of adhesion promoter enhanced coating adhesion to the substrates in both as-deposited samples and the ones heat-treated at 150 °C. In contrast, the adhesion strength decreased when heat-treatment was performed at higher temperatures, even when the concentration of adhesion promoter was increased. Numerical analysis was used to assess the effect of parylene coating on the electrical performance of a typical implantable, wirelessly powered model device. The results demonstrated that the presence of the parylene layer not only preserved the wireless coupling between this device and the pickup probe, but also enhanced it. In addition to these favourable physiochemical improvements, parylene also promoted general *in vivo* brain compatibility and cell viability of the devices. This study revealed the synergistic effects of pre- and post-deposition treatments and systematically optimized adhesion and stability of parylene coatings for implantable BMIs for the first time.

Received 1st July 2025
Accepted 21st July 2025

DOI: 10.1039/d5ra04683a

rsc.li/rsc-advances

Introduction

The development of implantable brain–machine interfaces (BMIs) has progressed significantly, enabling a wide range of functions, including neural recording, deep brain stimulation, imaging, drug delivery, and treatment of brain and neurological disorders.[1–5] Implantable bioelectronic devices are predominantly composed of metals and semiconductors, which are classified as inorganic materials. However, the inherent susceptibility of these materials to corrosion or degradation causes device failure, particularly in the harsh physiological environments, where they come into direct contact with body fluids. This unavoidably results in multiple surgeries for removing the failed device and replacing it with a new functional one. Furthermore, corrosion products may induce toxicity and inflammation in the host physiological environment.[6,7]

Parylene C is a derivative of parylene, in which poly(*para*-xylylene) is substituted with a single chlorine molecule, and has

[a]*Materials Science and Engineering, School for Engineering of Matter, Transport and Energy, Arizona State University, Tempe, AZ 85287, USA. E-mail: hamed.arami@asu.edu*

[b]*Biological Design Program, School for Engineering of Matter, Transport and Energy, Arizona State University, Tempe, AZ 85287, USA*

[c]*School of Electrical, Computer and Energy Engineering, Arizona State University, Tempe, AZ 85287, USA*

[d]*Chemical Engineering, School for Engineering of Matter, Transport and Energy, Arizona State University, Tempe, AZ 85287, USA. E-mail: layla.zadeh@asu.edu*

† Electronic supplementary information (ESI) available. See DOI: https://doi.org/10.1039/d5ra04683a

© 2025 The Author(s). Published by the Royal Society of Chemistry

Open Access Article. Published on 28 July 2025. Downloaded on 10/26/2025 10:23:19 AM.
This article is licensed under a Creative Commons Attribution-NonCommercial 3.0 Unported Licence.

been widely used for encapsulating and conformal coating of implantable medical devices.[8–11] It is a semi-crystalline polymeric coating known for excellent biocompatibility, chemical stability (highest among other types of parylene), high durability, low moisture absorption, and water impermeability.[12,13] Consequently, it offers long-lasting protection for implanted devices against enzymes and lipids in the corrosive environment of body.[14,15] While certain inorganic or ceramic materials offer superior dielectric properties, the selection of an encapsulation material for implantable devices should also account for conformality, biocompatibility, chemical resistance, and mechanical flexibility. Parylene is FDA-approved,[16] chemically inert, and has a long clinical history as a conformal barrier layer for medical implants. Its gas-phase deposition through chemical vapor deposition (CVD) enables uniform conformal encapsulation of high-aspect-ratio structures, and its mechanical flexibility ensures compatibility with both rigid and soft tissue interfaces.[17] The significant challenge associated with this promising coating is its weak adhesion to inorganic materials and high risk of delamination which can lead to disruption of device functionality after a short period of implantation.[14,18] This limitation arises from the inability of parylene to form a chemical bond with inorganic materials such as silicon and metals, which are leading candidates for implantable bioelectronics owing to their favorable electrical and mechanical properties.[14,18,19] To address this issue, we used 3-(trimethoxysilyl)propyl methacrylate, also called silane A-174 as an adhesion promoter. This molecule forms covalent bonds with both organic and inorganic materials. Trimethoxysilane group in the molecular structure of this promoter forms a covalent bond with hydroxyl groups on the substrates, and its methacrylate functional group polymerizes with the *para*-xylylene radicals in parylene molecules. These bondings can potentially improve the adhesion of parylene coating to the surface of substrates and generally prolong the lifetime of the implanted devices. This agent can be feasibly applied to substrates in both liquid (*e.g.*, dip-coating) and gas (*e.g.*, vacuum deposition) phases.[12,20,21] On the other side, the

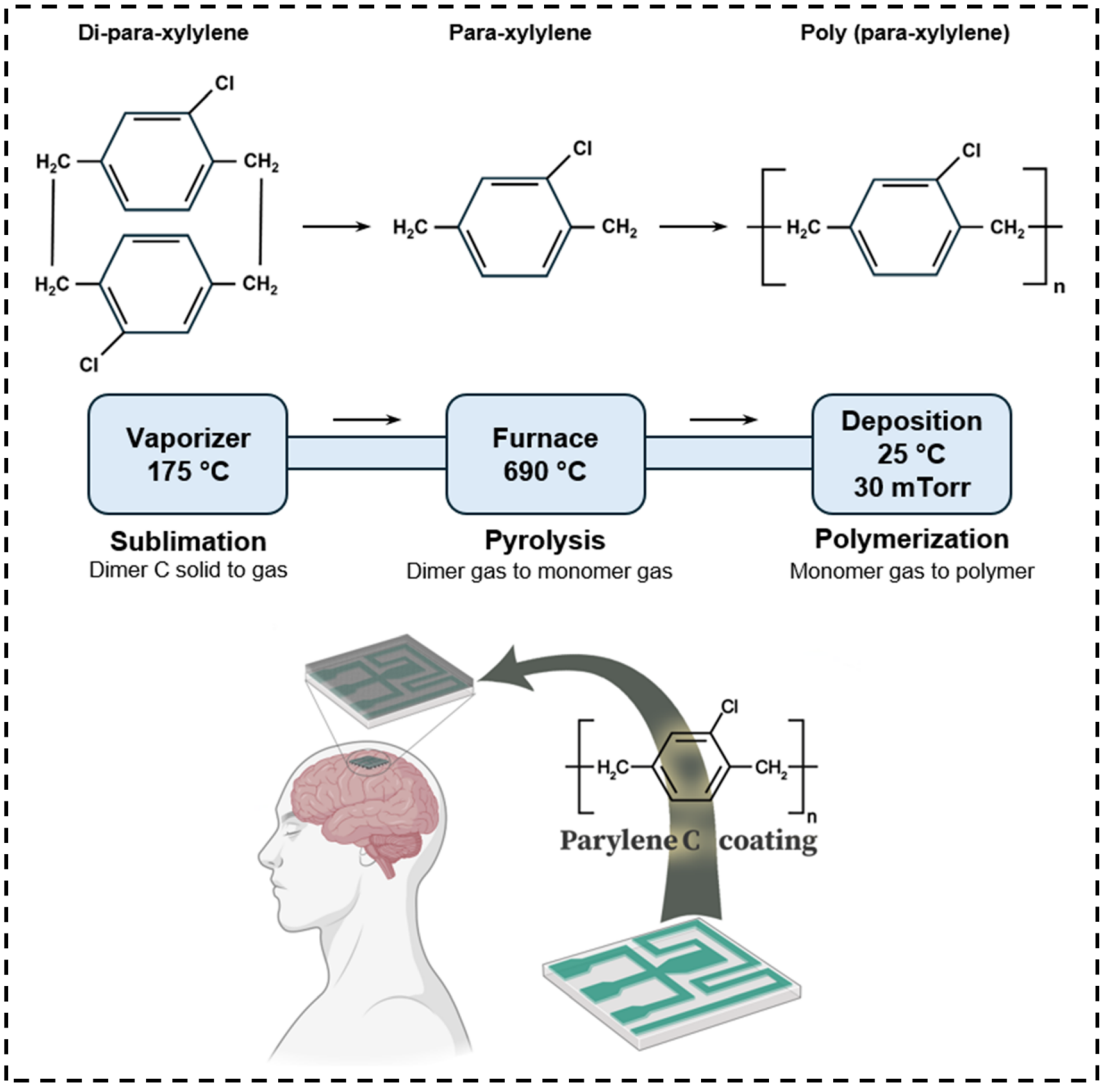

Scheme 1 Schematic showing the chemical mechanism and method used for encapsulating the neural devices with parylene C.

Open Access Article. Published on 28 July 2025. Downloaded on 10/26/2025 10:23:19 AM.
This article is licensed under a Creative Commons Attribution-NonCommercial 3.0 Unported Licence.

physiochemical properties of parylene C is highly dependent on its crystalline structure. Therefore, any process (*e.g.*, heat treatment) that can alter the crystallinity of parylene C, can modify its physiochemical properties after implantation.[22] Previous studies have shown that mechanical properties, such as Young's modulus and hardness of parylene C, can be increased through controlled heat treatments.[22,23] However, heat treatments in air and at temperatures exceeding 180 °C result in oxidation of parylene C and changes in its properties.[22,23] This oxidation can trigger the parylene C delamination through transformation of methylene bonds to ester bonds, making the devices vulnerable to hydrolysis in *in vivo* environments.[18,22] Moreover, heat treatments at or beyond 350 °C lead to decomposition of parylene C even in inert atmospheres such as nitrogen or argon.

The stability issues related to parylene coating are still a major drawback, especially for brain implants. Although previous studies have explored the use of silane adhesion promoters or post-deposition heat treatments independently to address this challenge, the combined and systematic study of both parameters across multiple levels has not been investigated. This work fills that gap by revealing interdependent effects between silane concentration and annealing temperature, evaluating their impact on parylene adhesion and coating integrity under physiologically related conditions, and systematically optimizes these parameters. These insights are essential for advancing the reliability of parylene coatings in long-term implantable systems.

Here, we provide a comparative experimental analysis to improve parylene coating for brain implantable devices and our findings can also be generalized for devices designed for other organs. We present synergistic effects of silanization and heat-treatment parameters (*i.e.*, different concentrations of the adhesion promoting agent, and post-deposition heat treatments temperatures), and coating thickness, on physiochemical stability and adhesion strength of parylene for brain implantable devices. We used various concentrations of 3-(trimethoxysilyl)propyl methacrylate (0%, 0.5%, 1%, and 1.5% (v/v)) to investigate its impact on the parylene coating adhesion to substrates. Then, we did heat treatments at 150, 200, and 250 °C in inert argon atmosphere to evaluate effects of annealing temperatures on mechanical strength and chemical stability of these coatings. The mechanical properties and adhesion strength of the coatings were also evaluated using a standard tape test (ASTM D3359). All samples were tested in an *in vitro* accelerated aging environment (phosphate-buffered saline (PBS) at elevated temperature (85–90 °C) for 7 days) to characterize their long-term stability in biological environments. Various devices (including rigid silicon or flexible polyimide) with optimal coating characteristics were used for cytotoxicity and brain compatibility (histology) evaluations. Finally, the potential impact of this optimized parylene encapsulation on the performance of a model wirelessly-operated implantable sensor was investigated using numerical simulations. This comparative study presents a roadmap for utilizing parylene coatings as an effective encapsulation layer on various types of substrates for chronic *in vivo* applications (Scheme 1).

Results and discussion

XRD and FT-IR analysis

Fig. 1(a) presents the FT-IR spectrum of the as-deposited parylene C. All spectral bands and functional groups are labeled in Fig. 1(a) and were compared with previous studies. Also, notable bands in this region are summarized in Table 1. The absence of an absorption band around 1700 cm^{-1} (in the range of 1675 cm^{-1} to 1740 cm^{-1}) implied that there were no carbonyl bands in the as-deposited film. The formation of carbonyl group in the FT-IR spectrum of parylene C is a sign of thermal oxidation.[24] These observations are in accordance with the results of Xu *et al.*,[25] in which the presence of carbonyl and carboxyl peaks were attributed to thermal and photo-oxidation of parylene C thin films, respectively. IR spectra for as-deposited parylene C and samples after heat treatment at different temperatures are compared in Fig. 1(b).

As parylene is a semi-crystalline polymer, any changes in the crystalline fraction of the structure of this material can change the physiochemical and mechanical properties of this material. Therefore, post-deposition heat treatments can play a key role in optimization of parylene coatings.[22,23] We annealed the samples at 150 °C, 200 °C, and 250 °C and investigated the effect of annealing temperature on the physiochemical and adhesion strength of the parylene coating. We chose 150 °C as the start point for annealing since it is close to crystallization temperature (T_C) of parylene C.[18] The differences in absorption intensity at different wavenumbers indicated the rearrangement of bonds and functional groups. The annealing procedure was performed in an argon atmosphere, and the spectra indicated that the annealed samples showed negligible signs of oxidation. In addition, we compared the IR spectra for each sample before and after the accelerated aging process, as illustrated in Fig. 1(c–f), to investigate the probability of parylene C oxidation under conditions simulating a physiological environment. A comparison of the as-deposited FTIR spectra (Fig. 1(c)) with annealed samples (Fig. 1(d–f)) implies that there is a deviation in the frequency range related to carbonyl bonds in as-deposited samples and the ones heat-treated at 200 °C. The observed deviations in the samples annealed at 200 °C (Fig. 1(e)) is attributed to changes in the vibrational modes of the molecules and rearrangements of the bonds. However, the deviation in the as-deposited samples after aging suggests potential oxidation, as no peak was observed in that spectral region before aging.[27,28] These observations implied that annealing of parylene C at these temperatures significantly increased the chemical stability of the parylene coating.

Fig. 2(a) presents the XRD patterns of the parylene C film for as-deposited and heat-treated samples. Parylene C is a semi-crystalline material consisting of both crystalline and amorphous phases in its structure. XRD patterns for all samples exhibited a peak around $2\theta \approx 14°$, which corresponds to the (020) plane.[22,26] The volume fraction of each phase varies with deposition conditions such as deposition rate, pressure, and temperature gradient inside the deposition chamber. The crystallinity also changes with post-deposition heat

 © 2025 The Author(s). Published by the Royal Society of Chemistry

Open Access Article. Published on 28 July 2025. Downloaded on 10/26/2025 10:23:19 AM.
This article is licensed under a Creative Commons Attribution-NonCommercial 3.0 Unported Licence.

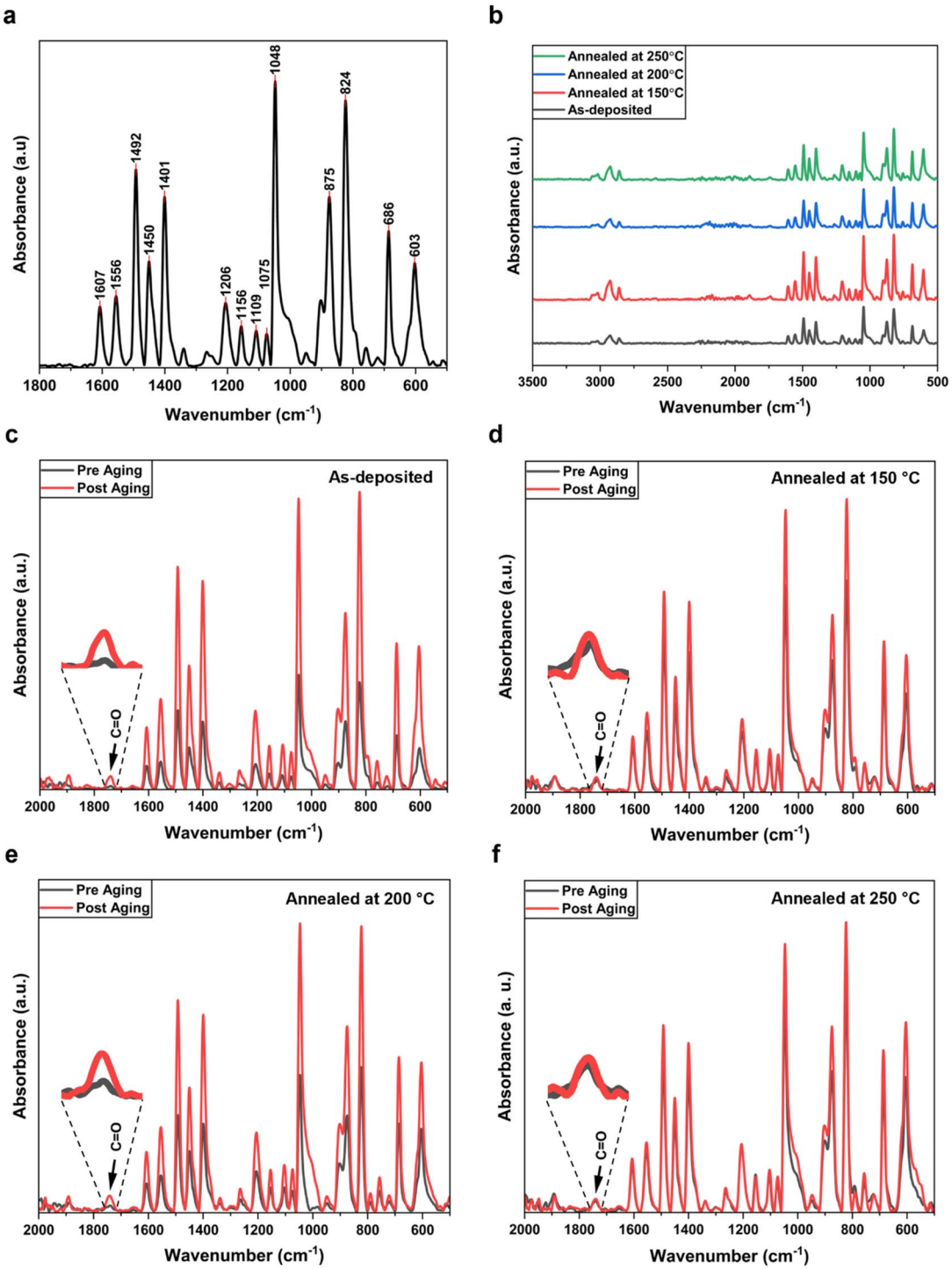

Fig. 1 FT-IR Spectra of parylene C deposited on silicon substrate before and after heat treatments and accelerated aging process. (a) As-deposited parylene C. (b) Comparison of FT-IR spectra for as-deposited samples and those subjected to heat treatment at various temperatures for 1 h after deposition. Differences in absorbance intensities of different peaks indicate rearrangement of bonds and functional groups as a result of heat treatment. (c–f) Comparison of FT-IR spectra before and after the accelerated aging process for (c) as-deposited parylene C, and samples subjected to post-deposition heat treatments at (d) 150 °C, (e) 200 °C, and (f) 250 °C for 1 h. The arrows show variations of carbonyl bonds in each sample.

treatments.[22,27,28] Diffraction patterns of all samples were analyzed using Bragg's and Scherrer's equations, and the calculation results are presented in Table 2. Fig. 2(a) shows that the height of the peak at $2\theta \approx 14°$ increased and the FWHM decreased, when samples were heat treated at higher temperatures. As illustrated in Fig. 2(b), sharper peaks were observed at

Open Access Article. Published on 28 July 2025. Downloaded on 10/26/2025 10:23:19 AM.
This article is licensed under a Creative Commons Attribution-NonCommercial 3.0 Unported Licence.

Table 1 The major FT-IR spectrum peaks of parylene C

Assignment	Wavenumber (cm^{-1})
C–C aliphatic bonds	603
H atoms bonded to an aromatic ring neighboring chlorine and ethyl group	823
Cl bonded to an aromatic ring	875 and 1048
In-plane deformation of C–H bond in aromatic ring (CH_2/CH)	1000–1200
CH_3 symmetric bending vibrations	1340
C–C deformation vibrations	1401
CH_2	1450
C–C ring stretching vibrations	1492
Skeletal aromatic C–C vibrations	1556 and 1607
Carbonyl	1675–1740
Aliphatic C–H stretch	2850–2950
Aromatic C–H stretch	3000–3100

higher temperatures, indicating increased crystallinity and growth in crystallite size. Moreover, the interlayer distance (*d*-spacing) decreased with elevation of heat treatment temperature (Fig. 2(b)). This phenomenon implies that more ordered polymer chains were formed at higher heat treatment temperatures. As illustrated in Fig. 2(b), the crystallinity and crystallite size did not exhibit a linear increase with increasing heat treatment temperature above 200 °C, because of proximity to the melting point of parylene C (290–300 °C).[22,29] Similarly, Hukins *et al.* and Huff *et al.* also reported that the crystallinity of parylene C decreases significantly, and parylene C diffraction patterns show a completely amorphous structure when the

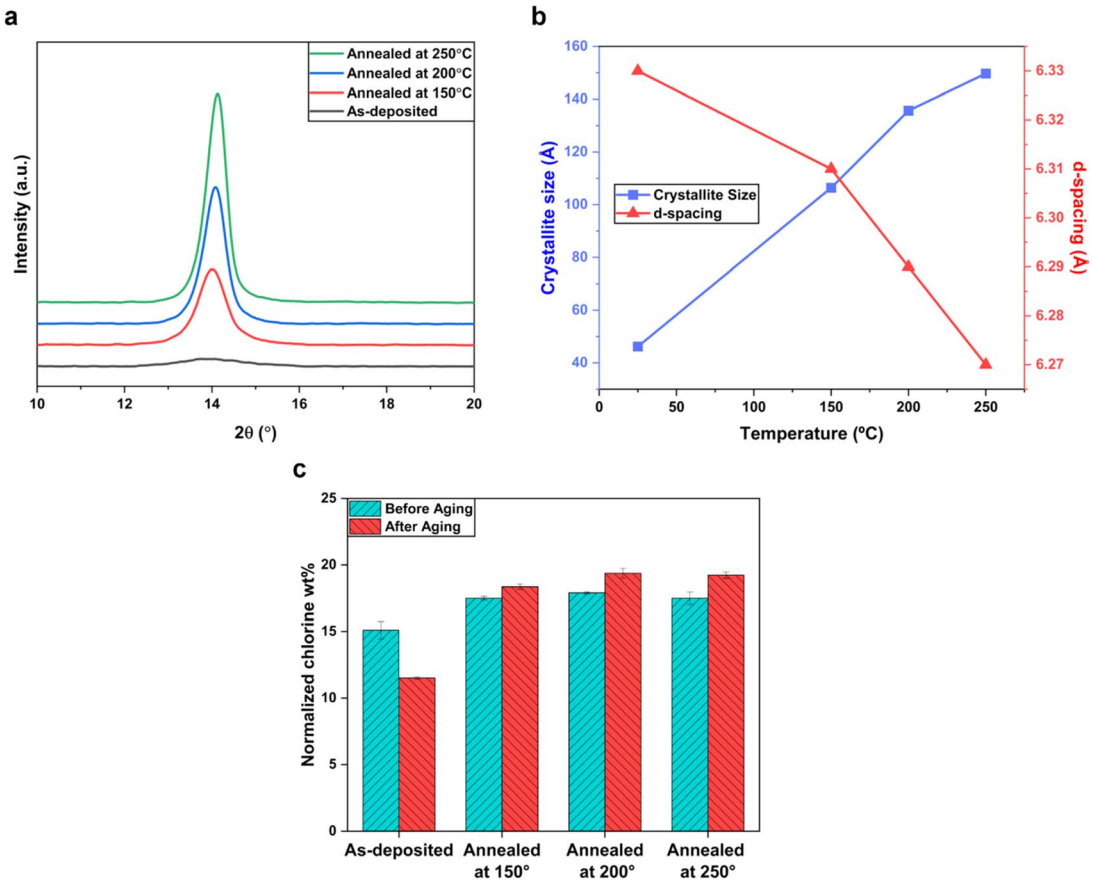

Fig. 2 (a) XRD patterns of parylene C films before and after heat treatment at different temperatures, showing higher crystallinity in samples heat treated at higher temperatures. (b) Changes in crystallite size and *d*-spacing with heat treatment temperature, calculated according to Scherrer's and Bragg's laws, respectively. (c) Ratio of chlorine-to-carbon atomic percentages obtained from EDS analysis of samples before and after the accelerated aging process for the as-deposited samples and samples subjected to post-deposition heat treatment at 150 °C, 200 °C, and 250 °C for 1 h. The results demonstrated chlorine abstraction, suggesting structural decay during the accelerated aging process for the as-deposited sample.

 © 2025 The Author(s). Published by the Royal Society of Chemistry

Open Access Article. Published on 28 July 2025. Downloaded on 10/26/2025 10:23:19 AM.
This article is licensed under a Creative Commons Attribution-NonCommercial 3.0 Unported Licence.

Table 2 XRD analysis of samples with identical deposition conditions, but varying heat treatment parameters

Sample	Peak center ($2\theta^{\circ}$)	Relative peak height	FWHM ($2\theta^{\circ} \times 10^{-3}$)	*d*-Spacing (Å)	Crystallite size (Å)
As-deposited	14	1	30	6.33	46.2
Annealed at 150 °C	14.04	9.8	13	6.31	106.4
Annealed at 200 °C	14.08	17.7	10	6.29	135.7
Annealed at 250 °C	14.12	27.1	9	6.27	149.7

temperature gets closer to 300 °C, and their observations were confirmed by DSC analysis of parylene C.[30,31]

EDS analysis

Fig. 2(c) shows the changes in the normalized chlorine-to-carbon atomic ratio. A chlorine abstraction was observed after the accelerated aging process for as-deposited samples, indicating degradation in the parylene C molecular structure. Parylene C has one chlorine atom per repeating unit of its chemical structure.[32] Therefore, any decrease in the normalized chlorine-to-carbon ratio can suggest parylene C degradation.[30] In contrast, no chlorine abstractions were observed in annealed samples, implying that post-deposition heat treatment can effectively improve the chemical stability of parylene C.

Surface morphology analysis

Fig. 3 illustrates optical microscopy images of the deposited parylene C on silicon substrates after the accelerated aging process. Details of all samples, including the thickness and pre- and post-deposition treatments, are presented in Table 3. Fig. 3(a–d) shows the effect of heat treatment temperature on the chemical stability and the adhesion strength of parylene C coatings. The greatest amount of delamination and the highest number of microcracks appeared in the as-deposited samples. Surface microscopy showed that the number of defects, including microcracks and delamination, was effectively reduced with heat treatment at 150 °C. However, these defects reappeared in heat-treated samples at higher temperatures. Fig. 3(c) demonstrates signs of micro-delamination and microcrack initiation in samples subjected to heat treatment at 200 °C. These defects developed into a greater number of grown microcracks and larger areas of delamination in heat-treated samples at 250 °C (Fig. 3(d)).

Comparison of Fig. 3(e–g) with Fig. 3(a, d, and h) showed the effects of heat treatments at different temperatures in the presence and absence of the adhesion promoter layer. These observations indicated that the adhesion promoter enhanced the adhesion strength and stability of the as-deposited coatings. Increasing the adhesion promoter concentration significantly reduced the number of defects, however, in heat-treated samples at 250 °C, its presence led to a rise in microcracks and delaminated spots. These defects furtherly increased at higher adhesion promoter concentrations in heat treated samples at 250 °C (Fig. 3(g, i, k, l)). Delamination and microcracks were observed both near the edges and in the central regions of the samples. These failure modes were especially pronounced in non-heat-treated samples, suggesting less chemical stability and increased susceptibility to moisture ingress through corroded regions, microdefects or imperfect edge coverage. Lower magnification microscopy images are also presented in Fig. S1.†

Mechanical properties of thin film

Fig. 4 presents the stereo microscopy images of the samples, in accordance with the ASTM D3359 standard tape test results, for samples subjected to various pre- and post-deposition treatments. The details of each sample, including thickness and pre- and post-deposition treatments, are presented in Table 4.

A comparison of Fig. 4(a) and (e) shows that increasing the coating thickness reduces the adhesion of the deposited thin film to the substrate, resulting in more delamination. This behavior is attributed to higher residual stress in thicker coatings, caused by differences in the thermal expansion coefficients and shrinkage rates of the coatings and substrates during deposition and heat treatments.[31] A comparison of Fig. 4(a) and (i) highlights the substantial impact of the adhesion promoter on enhancing the coatings adhesion to the substrates. Additionally, post-deposition heat treatments at 150 °C increased the crystallinity of the coatings, which improved their adhesion to the substrate, as shown in Fig. S3(a),† compared to the as-deposited samples (Fig. 4(a)). However, heat treatment at higher temperatures reduced the adhesion strength of the coatings to the substrates (Fig. S3(b) and (c)†). This observation suggests that a higher fraction of the crystalline phase in the parylene C structure, resulting from heat treatments above 150 °C, increases the brittleness of the coatings, leading to higher residual stress and reduced adhesion strength.[33] The synergistic effects of adhesion promoter and heat treatment were also compared in samples presented in Fig. 4(b–d), indicating that increasing the heat treatment temperature caused more delamination in samples with 0.5% adhesion promoter. This phenomenon was also observed in samples with 1% (Fig. 4(f–h)) and 1.5% (Fig. 4(j–l)) adhesion promoter. These comparisons imply that the adhesion promoter negatively impacted the adhesion strength of the coatings that were heat treated at 200 and 250 °C. The boiling point of 3-(trimethoxysilyl)propyl methacrylate is approximately 190 °C. As a result, the adhesion promoter is expected to decompose during the heat treatment at 200 and 250 °C, which accounts for its adverse effect on the adhesion strength of the coatings. While this study was conducted using flat, unetched samples, this choice was intentional to allow systematic evaluation of the effects of silane concentration and heat treatment on the chemical and mechanical stability of the coating, without the added

Open Access Article. Published on 28 July 2025. Downloaded on 10/26/2025 10:23:19 AM.
This article is licensed under a Creative Commons Attribution-NonCommercial 3.0 Unported Licence.

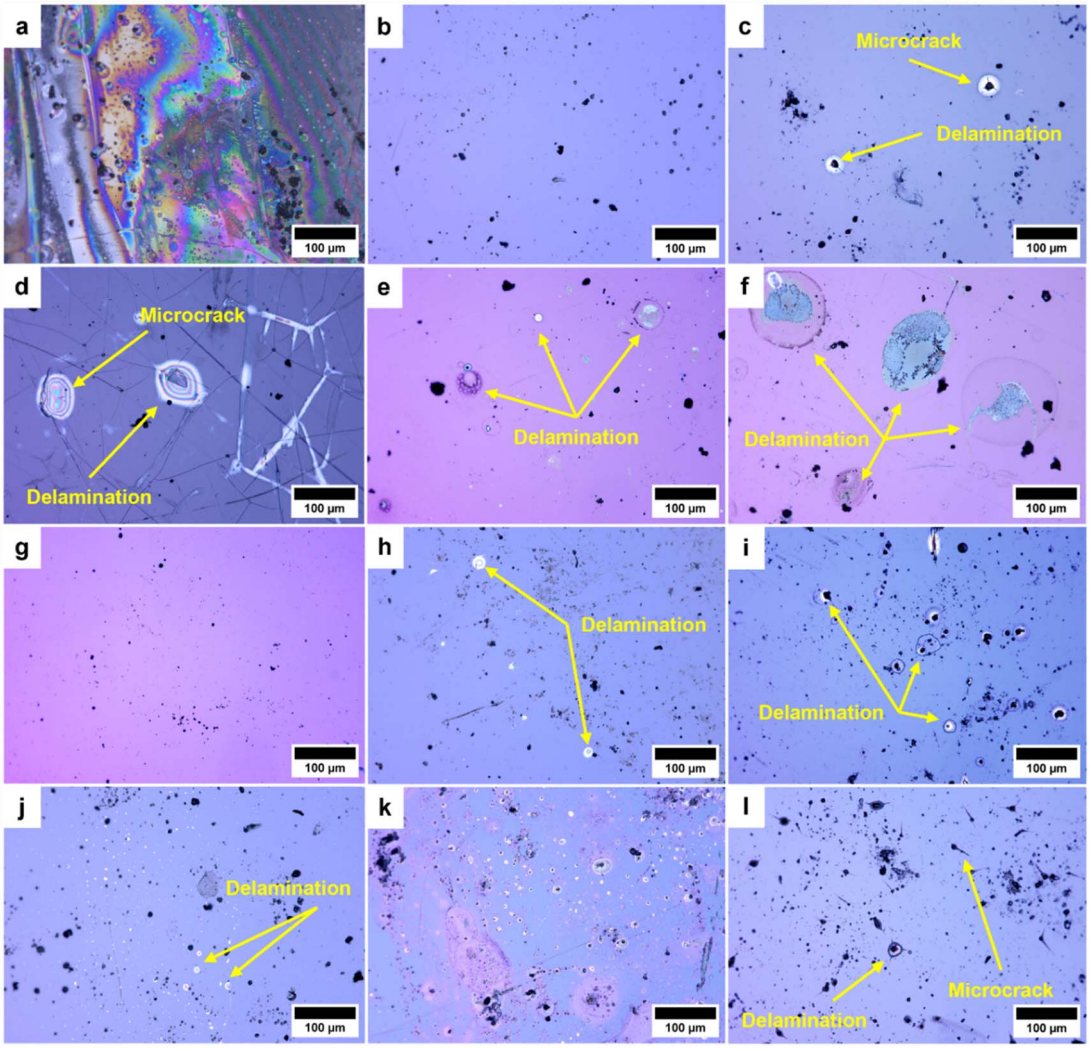

Fig. 3 High resolution optical microscopy images of a library of parylene coated samples after the accelerated aging process. Yellow arrows show the defects formed during the aging process. The fabrication details of each sample are summarized in Table 3 (Also see Fig. S1†).

Table 3 Summary of the parameters used for fabrication of the shown in Fig. 3

Sample	Thickness (μm)	Adhesion promoter concentration (%)	Heat treatment temperature (°C)
a	3	0	—
b	3	0	150
c	3	0	200
d	3	0	250
e	1	0	—
f	1	0	250
g	1	1.5	—
h	3	1.5	—
i	3	1	250
j	3	1	—
k	3	1.5	250
l	3	0.5	250

complexity of geometric features. Generally, parylene can be deposited on devices with various geometries and sizes *via* a CVD on-surface polymerization process, which enables highly conformal coating of complex geometries, including high-aspect-ratio features such as vias and trenches. As such, the trends observed in this work are expected to be generalizable to more complex device architectures. Furthermore, in practical device fabrication workflows, parylene encapsulation is typically performed after complete device assembly, ensuring that the final polymer coating conforms to all exposed surfaces and structural features, including interconnects and etched vias, which are often sources of gross interfacial failure.

In conclusion, the observed failure behaviors can be understood as the result of a combination of interfacial chemistry and annealing induced structural changes. Heat treatment at 150 °C increases crystallinity, which improves cohesion and reduces microdefect formation. However, at higher temperatures, silane thermal degradation (due to its ~190 °C boiling point) compromises interfacial bonding, while increased crystallinity introduces brittleness and internal stress inside the coating

 © 2025 The Author(s). Published by the Royal Society of Chemistry

Open Access Article. Published on 28 July 2025. Downloaded on 10/26/2025 10:23:19 AM.
This article is licensed under a Creative Commons Attribution-NonCommercial 3.0 Unported Licence.

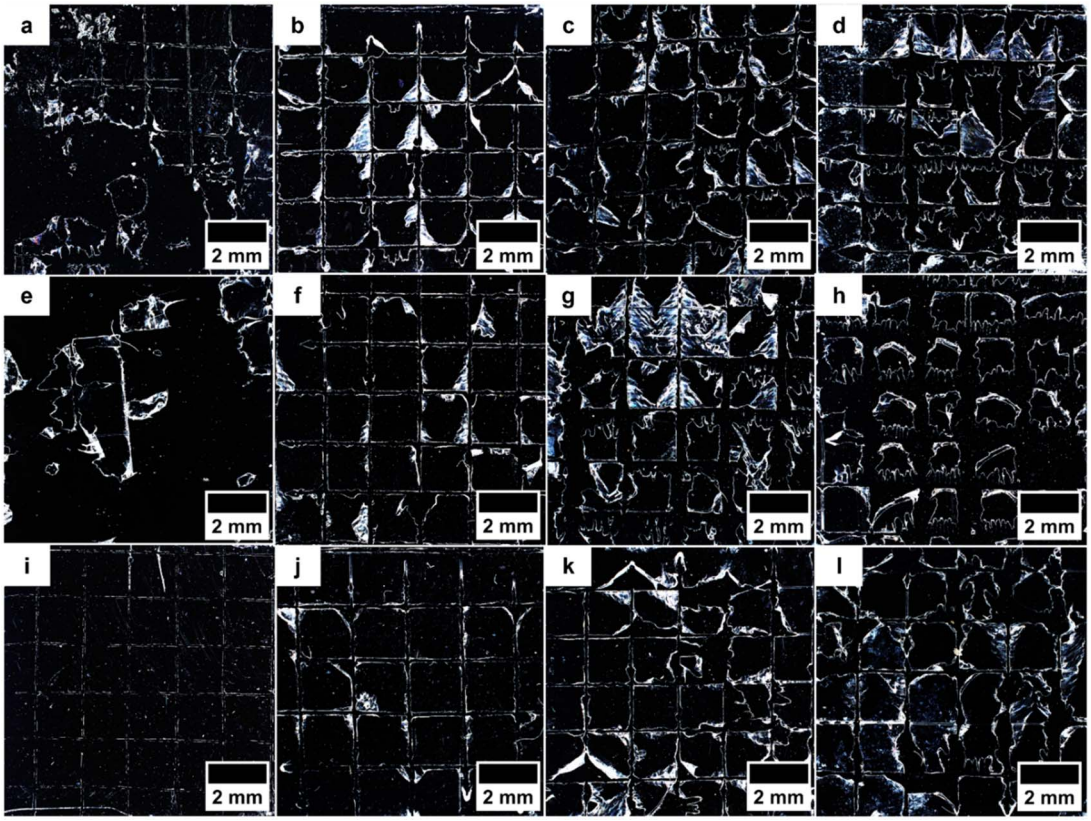

Fig. 4 Evaluation of adhesion strength using ASTM D3359 standard tape test for samples after the accelerated aging process. Fabrication details of each sample are summarized in Table 4. (a and e) Increasing the thickness of coatings led to lower adhesion strength and more delamination. (a and i) The adhesion promoter had a significant effect on the adhesion strength of the coating. (b–d) Increasing the heat treatment temperature increased the delamination in samples prepared with 0.5% adhesion promoter (Also see Fig. S2†).

Table 4 Fabrication details of the samples tested by the ASTM D3359 standard tape test shown in Fig. 4

Sample	Thickness (μm)	Adhesion promoter concentration (%)	Heat treatment temperature (°C)
a	1	0	—
b	3	0.5	150
c	3	0.5	200
d	3	0.5	250
e	3	0	—
f	3	1	150
g	3	1	200
h	3	1	250
i	1	0.5	—
j	3	1.5	150
k	3	1.5	200
l	3	1.5	250

layer. These changes promote delamination and microcracking. This interaction between chemical, mechanical, and structural factors provides insight into long-term encapsulation reliability for implantable devices.

In vitro biocompatibility test

Implantable medical devices, particularly bioelectronics tailored for diverse clinical functions, are in direct contact with biological tissues. Consequently, it is essential to thoroughly evaluate their physicochemical properties and biocompatibility prior to pre-clinical testing. Among the initial biological evaluations, *in vitro* cytotoxicity assays serve as a primary indicator of the biocompatibility of devices. Specifically, the MTT assay is widely employed to determine cell viability following direct exposure to fabricated devices, offering a reliable and quantitative assessment of cytotoxicity.[34] In this study, the MTT assay was utilized to evaluate the cytotoxicity and encapsulation efficacy of parylene in both organic and inorganic-based bioelectronic devices. While the biocompatibility of parylene is well established in the literature, the goal of these experiments was not to reconfirm its inherent safety, but to evaluate whether our optimized coating process, including silane treatment and heat exposure, retains biocompatibility when applied to functional brain implantable devices. These devices may contain materials such as metals or semiconductors that pose cytotoxic risks without effective encapsulation.[35–37] Fig. 5 represents the results of the cytotoxicity tests conducted on three different experimental groups as representatives of various types of neural devices, including group A: uncoated and parylene-coated

Open Access Article. Published on 28 July 2025. Downloaded on 10/26/2025 10:23:19 AM.
This article is licensed under a Creative Commons Attribution-NonCommercial 3.0 Unported Licence.

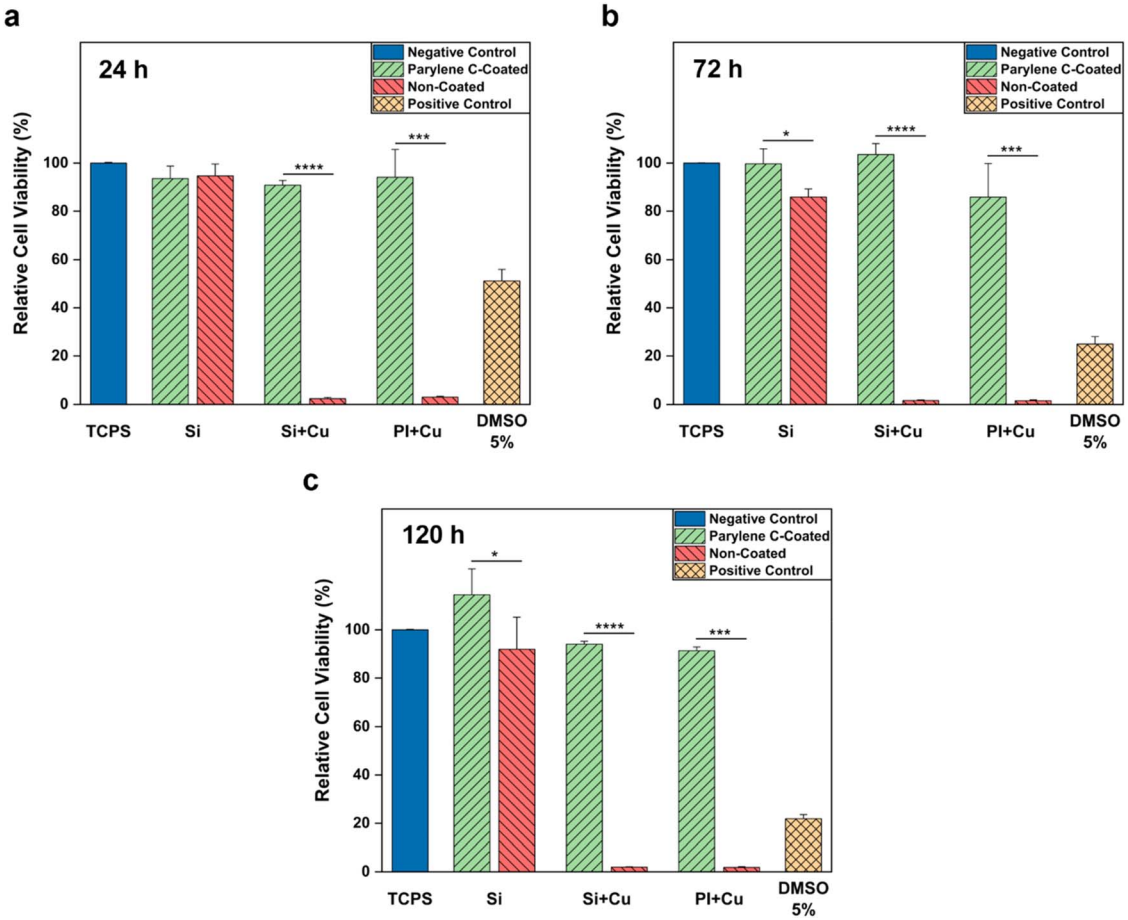

Fig. 5 Cytotoxicity of coated and uncoated silicon, copper trace–embedded silicon, and copper trace–embedded polyimide after incubation with NIH-3T3 cells for (a) 24 hours, (b) 72 hours, and (c) 120 hours. Results demonstrated the encapsulation efficacy of parylene for both flexible and rigid substrates. Data are shown as mean ± standard deviation, with experiments conducted in triplicate. Statistical significance was determined using one-way ANOVA followed by Tukey's post-hoc test for multiple comparisons; *$p < 0.05$, **$p < 0.01$, ***$p < 0.001$, ****$p < 0.0001$.

silicon substrates, group B: uncoated and parylene-coated copper trace-embedded silicon substrates, and group C: uncoated and parylene-coated copper trace-embedded polyimide substrates. Silicon-based samples served as representative models for rigid implantable bioelectronics, while polyimide-based samples represented flexible bioelectronics. NIH-3T3 fibroblast cells were used as the biological model for investigating cell viability. The cytotoxicity results across all groups and time points (24, 72, and 120 h) consistently demonstrated enhanced cell viability for parylene-coated substrates compared to their uncoated counterparts, confirming the cytocompatibility and effective encapsulation performance of the parylene coating. For group A, no significant difference in cell viability was observed between the parylene coated and non-coated subgroups after 24 hours of incubation. However, after 72 and 120 hours, extracts from parylene coated substrates demonstrated significantly higher cell viability compared to the non-coated substrates, implying a cumulative protective effect over time, potentially by preventing the accumulation of degradation products. The impact of parylene coating was more pronounced in groups B and C, where parylene-coated samples showed markedly improved cell viability compared to their non-coated counterparts ($P < 0.01$). Copper is known to leach ions that are detrimental to cell viability. The dramatic contrast between coated and uncoated samples in these groups highlights the effectiveness of parylene as a biocompatible diffusion barrier, mitigating copper ion release and preserving cellular health. Specifically, NIH-3T3 cells exposed to parylene-coated samples in group B maintained viability levels above 90% at 24, 72, and 120 hours, whereas non-coated samples exhibited high cytotoxicity, indicating the release of toxic ions or degradation products from the copper-containing surfaces ($P < 0.0001$). Similarly, the parylene-coated samples in group C, demonstrated significantly enhanced cell viability compared to their non-coated equivalents ($P < 0.001$). These results confirmed that parylene C coating effectively serves as a biocompatible encapsulation layer, mitigating the toxic effects associated with both organic and inorganic substrates. These findings are aligned with the previous studies and our *in vivo* biocompatibility studies.[35–37] The PI-based samples included in this study were not evaluated for adhesion strength and were not subjected to pre-deposition

 © 2025 The Author(s). Published by the Royal Society of Chemistry

Open Access Article. Published on 28 July 2025. Downloaded on 10/26/2025 10:23:19 AM.
This article is licensed under a Creative Commons Attribution-NonCommercial 3.0 Unported Licence.

treatments, as A-174 silane treatment is not effective on polyimide due to its limited efficacy on non-hydroxylated polymeric surfaces. Parylene is expected to have sufficient adhesion to organic substrates such as polyimide owing to favorable surface interactions between polymers.[14,18] However, its long-term stability on flexible substrates such as polyimide needs further investigations. We evaluated the biocompatibility and encapsulation performance of parylene on flexible polyimide-based devices containing copper circuit to assess the broader applicability of the optimized parylene coating for flexible implantable bioelectronics as well.[38–41]

In vivo biocompatibility assessments

To further evaluate the biocompatibility of parylene C coating, coated devices were implanted on the right hemisphere of the mouse brain ($n = 3$), while the left hemisphere remained intact and considered as the control (Fig. 6(a)). In this study, a cortical surface implantation approach with minimal craniotomy was utilized to evaluate the biocompatibility and encapsulation efficacy of the coated devices. This method was selected as a less invasive alternative to intracortical implantation, enabling *in vivo* assessment of tissue response while reducing confounding factors such as insertion-related trauma, tissue disruption, and mechanical strain. By minimizing these variables, the surface implantation model allowed for a more direct evaluation of the biological response to the parylene coating itself. However, more detailed studies should be considered for each BMI based on its shape, size, implantation procedure, and anatomical location in the brain, to allow for a more precise evaluation of its biocompatibility. The implantation procedure was well tolerated by the animals, and no complications such as infection or head/neck muscle injury were observed during or after implantation. Additionally, no behavioral abnormalities indicative of internal brain damage was detected during the 7 days period before euthanizing. As shown in Fig. 6(b and c), H&E staining was employed to assess tissue morphology, structural

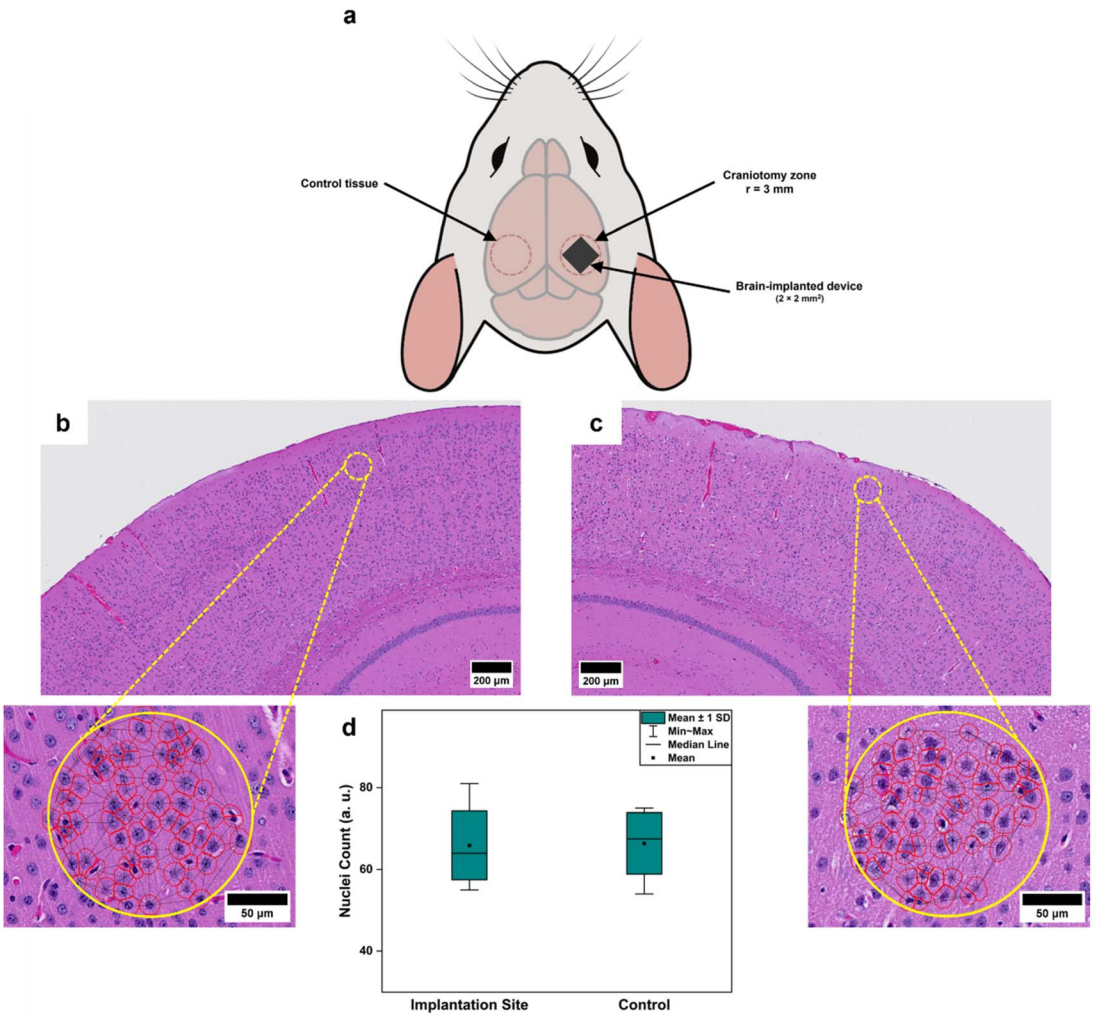

Fig. 6 Histological analysis of H&E-stained brain slices, comparing an area of the brain in the left hemisphere and far from implantation site as control (b), with an area adjacent to the implanted device (c). Quantitative analysis of cell nuclei counts at the implantation site *versus* the control tissue (d). Box plots represent the mean ± standard deviation, with whiskers representing the minimum and maximum values, and lines indicating the median. No statistically significant difference was observed between the two groups ($p > 0.05$), suggesting minimal inflammatory response following implantation.

Open Access Article. Published on 28 July 2025. Downloaded on 10/26/2025 10:23:19 AM.
This article is licensed under a Creative Commons Attribution-NonCommercial 3.0 Unported Licence.

integrity, and any signs of inflammation or cytotoxicity. Comparisons between control hemisphere (Fig. 6(b)) with tissue regions adjacent to the implanted device (Fig. 6(c)) indicated that the tissue architecture was relatively preserved, with well-defined cortical layers and normal cellular morphology around the implantation site. Additionally, a mild localized foreign body response with minimal inflammatory infiltration was observed, consistent with the cytotoxicity test results and further highlighting the biocompatibility of parylene C. Moreover, statistical comparison of nuclei counts between the implanted region and control tissue (Fig. 6(d)) revealed no significant difference ($p > 0.05$), indicating the absence of a severe immune response or increased cellular infiltration around the implantation site. These findings underscore the effectiveness of parylene C coating as an encapsulation layer for implantable bioelectronic devices, supporting its potential for safe and stable long-term neural interface applications.[35,37]

Numerical analysis

The primary functional mechanism of wirelessly implanted bioelectronic devices is the inductive coupling between the transmit and receive coils. Coating these devices can impact their performance by altering the reception of electromagnetic (EM) fields, as it introduces new boundary conditions for the propagated fields. To investigate the effects of parylene coating on the performance of wirelessly operated devices, full-wave EM simulations were conducted using HFSS Electronics Desktop. A previously reported wireless capacitive pressure sensor[42] without encapsulation was modeled (Fig. 7(b), top) and compared to a sensor coated with 2 μm of parylene (Fig. 7(b),

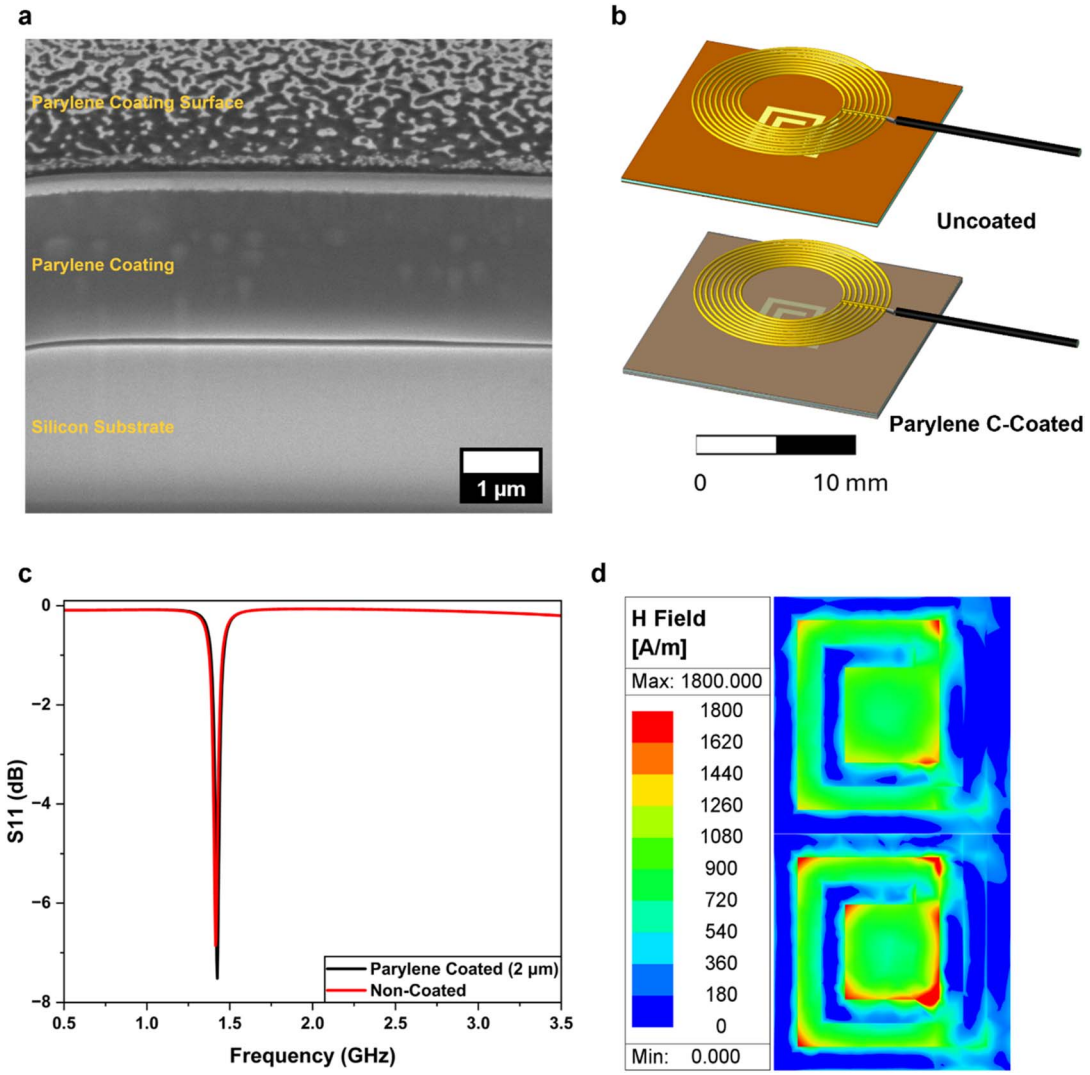

Fig. 7 (a) Cross-sectional SEM imaging showing 2 μm thick parylene coating on a silicon substrate. (b) Simulated uncoated (top) and parylene-encapsulated (bottom) pressure sensors used as model devices to evaluate effect of parylene coating on their wireless sensing performance. (c) Increased S11 parameter was observed after coating of the device, indicating stronger coupling between the pickup probe and the pressure sensor in the coated configuration. (d) H-field plots on the plane of uncoated (top) and parylene-encapsulated (bottom) pressure sensors further confirming the enhanced wireless performance after coating, because of stronger magnetic field reception at the device. Also, refer to Fig. S3† for details about effects of the thickness of parylene on wireless signal transfer efficiency.

 © 2025 The Author(s). Published by the Royal Society of Chemistry

Open Access Article. Published on 28 July 2025. Downloaded on 10/26/2025 10:23:19 AM. This article is licensed under a Creative Commons Attribution-NonCommercial 3.0 Unported Licence.

bottom), simulating a fully implantable bioelectronic device. Fig. 7(c) presents the calculated reflection coefficient (S11) for both uncoated and coated pressure sensors. The parylene-coated sensor demonstrated a higher return loss (−S11) of 7.52 dB at 1.42 GHz, compared to 6.85 dB at 1.41 GHz for the uncoated sensor, indicating stronger coupling between the pickup probe and the pressure sensor in the coated configuration. The H-field distribution on the plane of the uncoated (Fig. 7(d), top) and coated (Fig. 7(d), bottom) pressure sensors further confirmed the presence of a stronger magnetic field when parylene coating was applied. Fig. S4-a and b† show S11 data for sensors coated with 1 μm and 3 μm of parylene, compared to the uncoated sensor, indicating that higher return loss consistently occurred with parylene coating. A slight resonance frequency shift to higher frequencies was observed with the 1 μm parylene coating relative to the uncoated sensor, attributed to changes in boundary conditions introduced by the thinner parylene layer. In contrast, increasing the parylene thickness to 3 μm caused a shift to lower resonance frequencies due to an increased loading effect from the thicker coating.[43] As shown in Fig. S4(c) and (d)†, the H-field intensity consistently appeared stronger in the presence of parylene, regardless of the thickness. The is mainly because of generation of a secondary magnetic field by the dielectric layer (*i.e.*, parylene) at the surface of the device, which, in turn, can enhance the coupling between the sensor and the pickup probe.[43] The goal of this wireless device simulation was not to compare antenna stack designs (*e.g.*, PI-metal-PI *versus* PI-metal), but to evaluate whether parylene encapsulation would negatively impact electromagnetic coupling performance. The simulated structure was selected to only study the influence of the parylene coating, without introducing additional complexity from multilayer stack configurations. Simulation results demonstrated that the parylene coating with this thickness preserved, and even slightly improved, wireless signal transfer, confirming that it does not degrade the electromagnetic response of the system. These observations indicated potential electrical performance benefits for wireless BMIs.

Conclusions

This work aimed to tune characteristics of parylene as a clinically-relevant promising candidate for effective encapsulation of implantable brain–machine interfaces (*e.g.*, neural devices). We developed pre- and post-coating treatments that affect the chemical, physical, mechanical properties (*i.e.*, adhesion strength), and lifetime of the parylene coating. Our results demonstrated that controlled post-deposition heat treatment at 150 °C enhanced the chemical stability and mechanical strength of parylene C coatings by increasing its crystallinity. However, higher levels of crystallinity caused by heat treatments at temperatures above 150 °C, embrittled the coating, resulting in formation of defects and fast delamination due to the residual interfacial stresses caused by heat treatment. Additionally, increasing the coating thickness, decreased the adhesion and raised the risk of delamination and microcrack initiation/growth due to higher residual stress in the coating resulted from the differences in their shrinkage ratios and thermal expansion coefficients. The adhesion promoter significantly enhanced the coating adhesion in as-deposited samples and the ones heat-treated at 150 °C. However, the presence of adhesion promoter affected the adhesion strength after heat treatment at higher temperatures (>150 °C) negatively. This was because of possible degradation of this promoter layer, when samples were heated at higher temperatures. Cytotoxicity and histology studies showed improved cell viability and brain compatibility after encapsulation of the devices with parylene C. Numerical simulations demonstrated that parylene coating does not change the wireless signal transfer and functionality of the devices.

Data availability

The authors declare that the data supporting the findings of this study are available within the paper and its ESI File.†

Conflicts of interest

The authors declare no conflict of interest.

Acknowledgements

This work was in part supported by National Institute of Health (NIH, Grant No. 5R00EB031178-05, 5K99EB031178-02, 5R00CA234208-05, and 4K99CA234208-03). M. G., N. S., D. T. S., M. S., S. H. were supported by ASU College of Engineering Fulton Fellowship. Authors thank Dr Page Baluch for providing the NIH-3T3 cells. We acknowledge the helps from Lia Felix and Joshua Saunders for helping us to run some experiments. Also, we acknowledge the use of facilities within the Eyring Materials Center at Arizona State University supported in part by NNCI-ECCS-1542160.

Notes and references

1 P. Gutruf and J. A. Rogers, *Curr. Opin. Neurobiol.*, 2018, **50**, 42–49.
2 J. C. Barrese, N. Rao, K. Paroo, C. Triebwasser, C. Vargas-Irwin, L. Franquemont and J. P. Donoghue, *J. Neural Eng.*, 2013, **10**, 066014.
3 S. Venkatraman, J. Hendricks, Z. A. King, A. J. Sereno, S. Richardson-Burns, D. Martin and J. M. Carmena, *IEEE Trans. Neural Syst. Rehabil. Eng.*, 2011, **19**, 307–316.
4 H. Zhao, R. Liu, H. Zhang, P. Cao, Z. Liu and Y. Li, *Micromachines*, 2022, **13**, 386.
5 C. Hassler, R. P. Von Metzen, P. Ruther and T. Stieglitz, *J. Biomed. Mater. Res., Part B*, 2010, **93B**, 266–274.
6 G. Hong and C. M. Lieber, *Nat. Rev. Neurosci.*, 2019, **20**(6), 330–345.
7 P. K. Campbell, K. E. Jones, R. J. Huber, K. W. Horch and R. A. Normann, *IEEE Trans. Biomed. Eng.*, 1991, **38**, 758–768.
8 C. Hassler, R. P. Von Metzen, P. Ruther and T. Stieglitz, *J. Biomed. Mater. Res., Part B*, 2010, **93B**, 266–274.

Open Access Article. Published on 28 July 2025. Downloaded on 10/26/2025 10:23:19 AM.
This article is licensed under a Creative Commons Attribution-NonCommercial 3.0 Unported Licence.

9 M. Cieślik, S. Zimowski, M. Gołda, K. Engvall, J. Pan, W. Rakowski and A. Kotarba, *Mater. Sci. Eng., C*, 2012, **32**, 2431–2435.
10 A. A. Benbuk, H. Esmaeili, S. Liu, A. Patino-Guerrero, R. Q. Migrino, J. Chae, M. Nikkhah and J. Blain Christen, *ACS Sens.*, 2022, **7**, 3287–3297.
11 A. Kohler, F. Blendinger, S. Müller, U. Mescheder and V. Bucher, *Front. Med. Technol.*, 2023, **5**, 1211423.
12 S. Staufert, P. Gutzwiller, F. Mushtaq and C. Hierold, *ACS Appl. Nano Mater.*, 2018, **1**, 1586–1594.
13 J. Bavier, J. Cumings and D. R. Hines, *Microelectron. Eng.*, 2013, **104**, 18–21.
14 J. Charmet, J. Bitterli, O. Sereda, M. Liley, P. Renaud and H. Keppner, *J. Microelectromech. Syst.*, 2013, **22**, 855–864.
15 S. Minnikanti, G. Diao, J. J. Pancrazio, X. Xie, L. Rieth, F. Solzbacher and N. Peixoto, *Acta Biomater.*, 2014, **10**, 960–967.
16 E. Pierstorff, R. Lam and D. Ho, *Nanotechnology*, 2008, **19**, 445104.
17 X. Z. Xie, L. Rieth, P. Tathireddy and F. Solzbacher, in *Procedia Engineering*, 2011, vol. 25, pp. 483–486.
18 A. Kachroudi, C. Lagomarsini, V. H. Mareau and A. Sylvestre, *J. Appl. Polym. Sci.*, 2019, **136**(1), 46908.
19 Z. Song, J. H. Im, H. Ko, J. H. Park, G. Y. Lee, M. J. Kang, M. H. Kim and J. C. Pyun, *Mater. Today Commun.*, 2021, **26**, 101834.
20 S. van den Driesche, C. Habben, A. Bödecker, W. Lang and M. J. Vellekoop, *Proceedings*, 2017, **1**, 299.
21 J. Ortigoza-DIaz, K. Scholten and E. Meng, *J. Microelectromech. Syst.*, 2018, **27**, 874–885.
22 N. Jackson, F. Stam, J. O'Brien, L. Kailas, A. Mathewson and C. O'Murchu, *Thin Solid Films*, 2016, **603**, 371–376.
23 R. P. Von Metzen and T. Stieglitz, *Biomed. Microdevices*, 2013, **15**, 727–735.
24 G. Maggioni, A. Tessarollo and S. Carturan, *Mater. Chem. Phys.*, 2015, **149–150**, 530–538.
25 K. G. Pruden, K. Sinclair and S. Beaudoin, *J. Polym. Sci., Part A:Polym. Chem.*, 2003, **41**, 1486–1496.
26 M. A. Surmeneva, A. Vladescu, C. M. Cotrut, A. I. Tyurin, T. S. Pirozhkova, I. A. Shuvarin, B. Elkin, C. Oehr and R. A. Surmenev, *Appl. Surf. Sci.*, 2018, **427**, 617–627.
27 J.-M. Hsu, L. Rieth, S. Kammer, M. Orthner and F. Solzbacher, *Sens. Mater.*, 2008, **20**, 87.
28 E. M. Davis, N. M. Benetatos, W. F. Regnault, K. I. Winey and Y. A. Elabd, *Polymer*, 2011, **52**, 5378–5386.
29 S. Buchwalder, A. Borzì, J. J. Diaz Leon, F. Bourgeois, C. Nicolier, S. Nicolay, A. Neels, O. Zywitzki, A. Hogg and J. Burger, *Polymers*, 2022, **14**(17), 3677.
30 D. W. L. Hukins, A. Mahomed and S. N. Kukureka, *Med. Eng. Phys.*, 2008, **30**, 1270–1274.
31 M. Huff, *Micromachines*, 2022, **13**, 2084.
32 B. J. Kim and E. Meng, *Polym. Adv. Technol.*, 2016, **27**, 564–576.
33 S. J. A. Hocker, W. T. Kim, H. C. Schniepp and D. E. Kranbuehl, *Polymer*, 2018, **158**, 72–76.
34 L. Tolosa, M. T. Donato and M. J. Gómez-Lechón, *Methods Mol. Biol.*, 2015, **1250**, 333–348.
35 M. Madarász, F. Z. Fedor, Z. Fekete and B. Rózsa, *Front. Neurosci.*, 2023, **17**, 1209913.
36 Y. Kim, S. Alimperti, P. Choi and M. Noh, *Sensors*, 2022, **22**, 1277.
37 B. D. Winslow, M. B. Christensen, W. K. Yang, F. Solzbacher and P. A. Tresco, *Biomaterials*, 2010, **31**, 9163–9172.
38 V. Castagnola, E. Descamps, A. Lecestre, L. Dahan, J. Remaud, L. G. Nowak and C. Bergaud, *Biosens. Bioelectron.*, 2015, **67**, 450–457.
39 A. Lecomte, A. Degache, E. Descamps, L. Dahan and C. Bergaud, *Sens. Actuators, B*, 2017, **251**, 1001–1008.
40 A. T. Satti, J. Park, J. Park, H. Kim and S. Cho, *Sensors*, 2020, **20**, 5183.
41 S. Takeuchi, D. Ziegler, Y. Yoshida, K. Mabuchi and T. Suzuki, *Lab Chip*, 2005, **5**, 519–523.
42 S. Hashemi, S. Ebrahimibasabi, M. Sajjadi, N. Shahraki, D. Tamjid Shabestari, M. Golshahi, S. Zeinolabedinzadeh, H. Arami and L. Khalifehzadeh, *Adv. Mater. Technol.*, 2025, e01316.
43 S. Hashemi, S. K. Kandala, B. Agbo, Z. A. Colwell, K. Song, R. Xie and S. M. Sohn, *IEEE J. Electromagn. RF Microw. Med. Biol.*, 2023, **7**, 432–439.

 © 2025 The Author(s). Published by the Royal Society of Chemistry